Check for updates

TEM-compatible microdevice for the complete thermoelectric characterization of epitaxially integrated Si-based nanowires†

Jose M. Sojo-Gordillo, [ID] *[ab] Yashpreet Kaur, [ID] [b] Saeko Tachikawa,[bc] Nerea Alayo,[a] Marc Salleras, [ID] *[d] Nicolas Forrer, [ID] [b] Luis Fonseca,*[d] Alex Morata, [ID] *[a] Albert Tarancón [ID] *[ae] and Ilaria Zardo [ID] *[bf]

Nanostructured materials present improved thermoelectric properties due to non-trivial effects at the nanoscale. However, the characterization of individual nanostructures, especially from the thermal point of view, is still an unsolved topic. This work presents the complete structural, morphological, and thermoelectrical evaluation of the selfsame individual bottom-up integrated nanowire employing an innovative micro-machined device compatible with transmission electron microscopy whose fabrication is also discussed. Thanks to a design that arranges the nanostructured samples completely suspended, detailed structural analysis using transmission electron microscopy is enabled. In the same device architecture, electrical collectors and isolated heaters are available at both ends of the trenches for thermoelectrical measurements of the nanowire *i.e.* thermal and electrical properties simultaneously. This allows the direct measurement of the nanowire power factor. Furthermore, micro-Raman thermometry measurements were performed to evaluate the thermal conductivity of the same suspended silicon nanowire. A thermal profile of the self-heating nanowire could be spatially resolved and used to compute the thermal conductivity. In this work, heavily-doped silicon nanowires were grown on this microdevices yielding a thermal conductivity of 30.8 ± 1.7 W Km^{-1} and a power factor of 2.8 mW mK^{-2} at an average nanowire temperature of 400 K. Notably, no thermal contact resistance was observed between the nanowire and the bulk, confirming the epitaxial attachment. The device presented here shows remarkable utility in the challenging thermoelectrical characterization of integrated nanostructures and in the development of multiple devices such as thermoelectric generators.

New concepts

Our research introduces a groundbreaking micro-machined device designed for the comprehensive evaluation of individual bottom-up integrated nanowires, marking a significant advancement in science and nano-technology applied to silicon-based micro-thermoelectric devices. Current approaches rely on the extraction of the different structural, morphological and thermoelectric properties using different devoted samples. This hinders a straightforward cross-correlation of their properties due to the intrinsic variability across samples. In contrast, the novelty of our work lies in the unique microdevice design, which enables to measure all properties over the exact same epitaxially integrated nanowire. In particular, our device facilitates transmission electron microscopy experiments, allowing detailed morphological and structural analysis, while also featuring electrical collectors and heaters for a full thermoelectric characterization, including electrical and thermal conductivity as well as the Seebeck coefficient. In addition, this work introduces a completely new methodology to extract the light absorption coefficient of the nanowires using Raman thermography and, simultaneously, provides the first reported direct proof of null thermal contact resistance in a double-sided epitaxial nanowire integration. In summary, our work provides the first instance of epitaxially integrated nanowires being fully morphologically, structurally, and thermoelectrically characterized. This microdevice promises transformative applications in the challenging thermoelectrical characterization of integrated nanostructures and the development of diverse devices like thermoelectric generators.

[a] Catalonia Institute for Energy Research, IREC, Jardins de les Dones de Negre 1, 08930 Sant Adrià de Besòs, Barcelona, Spain. E-mail: jose.sojo@unibas.ch, amorata@irec.cat, atarancon@irec.cat

[b] University of Basel, Klingelbergstrasse 82, 4056, Basel, Switzerland. E-mail: ilaria.zardo@unibas.ch

[c] National Institute of Advanced Industrial Science and Technology, AIST, Tsukuba 1-1-1, Chuo Daisan Chuo Honkan 1F, Tsukuba, Japan

[d] Institute of Microelectronics of Barcelona, IMB-CNM (CSIC), C/Til·lers s/n, Campus UAB, Bellaterra, 08193, Barcelona, Spain. E-mail: marc.salleras@imb-cnm.csic.es, luis.fonseca@imb-cnm.csic.es

[e] ICREA, Passeig de Llúis Companys, 23, 08010 Barcelona, Spain

[f] Swiss Nanoscience Institute, SNI, Klingelbergstrasse 82, 4056, Basel, Switzerland

† Electronic supplementary information (ESI) available: Additional referenced figures and tables as well as details of the calibration process. See DOI: https://doi.org/10.1039/d4nh00114a

1 Introduction

In recent years, nanowires (NWs) have emerged as promising building blocks for applications in the fields of electronics,[1] optoelectronics,[2] photonics,[3] and energy conversion.[4–6] The latter is of great relevance, as the incoming development of the internet of things urgently demands locally available and non-intermittent energy sources to power the increasing amount of wireless devices connected.[7] The emergence of devices powered by micro thermoelectric (TE) generators featuring environmentally sound, cheap, and abundant silicon-based nanowires has, therefore, boosted theoretical and experimental studies on the optimization of their TE energy conversion.[8–10] This conversion efficiency is conveniently benchmarked by the figure-of-merit, $(zT = \sigma S^2/\kappa T)$, where S is the Seebeck coefficient, σ the electrical conductivity, and κ the thermal conductivity.[11] Hence, the optimal efficiency is achieved by a material of low thermal conductivity and high electrical conductivity.

While electronic property measurements are relatively simple to perform on NWs nowadays, evaluating the thermal conductivity remains challenging. Generally, employed techniques for measuring thermal transport properties of a single nanowire include the use of suspended nanocalorimeters.[12–18] This typically requires preparing and placing the sample of interest over the gap between the suspended platforms. The transfer of the sample is usually a tedious task that requires micro-manipulation techniques which are not easily accessible. Furthermore, the problem of thermal contact resistance persists in this measurement method, typically leading to an underestimation of thermal conductivity.[19,20]

Alternatively, the state-of-the-art characterization devices for integrated nanostructures are currently based on silicon-on-insulator (SOI) microfabricated trenches.[21] This integration approach – based on the epitaxial growth of the nanostructures directly on the test device – enables the electrical probing of the NWs while, at the same time, overcomes the problem of the thermal contact resistance.[22] However, most of these microfabricated test platforms are unsuitable for transmission experiments such as electron microscopy techniques (TEM) or other measurements affected by the substrate like Raman spectroscopy – where the underlying silicon substrate masks the faint signal of the nanowires. Additionally, the efficient thermal dissipation of bulk silicon drastically reduces the accuracy of Seebeck coefficient measurements using microheaters for driving controlled thermal gradients. The aforementioned drawbacks force to measure each property in different platforms, hindering a full morphological and TE characterization of the selfsame nanostructure.

In order to overcome these limitations, this work proposes a new multi-purpose test device (MPTD), enabling a full morphological, structural and TE study of an individual epitaxially integrated NW using accessible and non-destructive techniques. This enables cross-correlation studies where morphological and structural parameters can be quantified and directly related to observed changes in TE properties. The described integration pathway avoids sample transfer problems by allowing the direct growth of NWs in the test microdevice. Moreover, when full epitaxial integration is achieved, measurements are drastically simplified as contact resistance becomes negligible.[21] This MPTD features through-all trenches (all across the bulk) and presents a 3 mm-diameter dodecagonal shape that fits in conventional TEM sample holders. Additionally, the same trenches enable the NW measurement using micro-Raman analysis without suffering from any background signals. This work covers both a detailed discussion of the fabrication and the subsequent TE characterization of an integrated silicon NW.

2. Methods

2.1. NW growth

Boron-doped Si NWs were grown in a chemical vapor deposition (CVD) chamber (FirstNano Easytube 3000 LP-CVD system) through the vapor–liquid–solid (VLS) mechanism and employing gold nanoparticles as seeds.[23] Such NWs were integrated into the MPTD exhibiting exposed silicon walls presenting $\langle 111 \rangle$ surfaces as described later. Gold nanoparticles (NPs) – required for the formation of eutectic nanodroplets of Au–Si alloy that acts as a catalyst of the VLS process – were deposited using electrostatic colloidal drop cast,[24,25] creating a homogeneous and sparsed seed density with a high degree of control over the particle diameter. A commercial suspension of citrate-stabilized Au colloids (negatively charged) of 80 nm in diameter (Sigma Aldrich) and diluted poly-L-lysine (positively charged) at 0.1% to promote adhesion was employed. The sonication of the suspension prior to the electrostatic deposition was found essential in preventing the agglomeration of colloids. Further details of the process can be found in our prior works.[6,26] Additionally, a 20 min 5% hydrofluoric acid (HF) etch was performed before the NP deposition in order to remove the protective SiO_2 layer from the device surface.

Subsequently, the $\langle 111 \rangle$-aligned Si NWs were grown in a CVD reactor immediately after a second 5% HF acid etch (30 s) for removing the native oxide layer at the seeded Si surfaces.[25] Optimized CVD conditions for device-integrated Si NWs are detailed in our previous work.[26] The doping level of the Si NWs was controlled with the diborane partial pressure $(P_{B_2H_6})$ inside the CVD chamber, which is set by the input flow. A partial pressure of 10 mPa was used. In order to ensure a proper impurity activation, all devices with integrated NW samples were thermally annealed at 800 °C (ramps of 12 K min^{-1}) immediately after the VLS-CVD growth. This activation process also contributes to remove any rectifying effect at the metal–SOI interfaces.

Owed to the randomness of the Au catalyst deposition process, the growth position of NWs was not controlled. In order to ensure a single NW bridging a pair of cantilevers per chip, unwanted pairs of cantilevers were subsequently removed by pressing on them using microtips as illustrated in Fig. S1c (ESI†). Further details on the mechanical design of this feature is found in the ESI.†

2.2. Thermoelectric measurements

Electrical measurements were performed using Keithley 4200 A semiconductor analyzer featuring 4 source-meter units (SMU). During all measurements, the devices were loaded on a sealed heating stage within a Janis ST-500 probe station chamber at a vacuum pressure of (1×10^{4}–1×10^{5} mbar). TE characterization was carried out by performing electrical measurements of open circuit voltage (V_{OC}) and resistance (R_{HT}) of the heater/thermometer devices. Heater resistances were converted to ΔT using a temperature coefficient of resistance (TCR) calibrated prior to the measurements and further confirmed using Raman thermography (details below). A stabilization time of 120 s between different current biases applied and subsequent V_{OC} readouts ensured thermal stabilization of the device at each temperature step. Electrical conductivity measurements were conducted by performing current–voltage (I–V) curves of the NWs in a 4-wire configuration.

Thermal conductivity was measured by probing the NW local temperature along the longitudinal axis with a 532 nm laser using Raman thermography[27,28] while heating the wire with the Joule dissipated heat produced by a bias current applied to it. The spot size of the laser beam was estimated to be $\sim$872 nm using the $1/e^2$ definition with a numerical aperture NA = 0.5 of the objective (Mitutoyo 100X with 12.13 mm working distance). A Princeton Instrument single spectrometer (1800 g mm^{-1}) featuring an Andor iDus 416A CCD camera was used for the Raman spectra acquisition, providing a spectral resolution of 0.32 cm^{-1} per pixel. All spectra used for the thermal evaluation were acquired with integration times of 5×50 s with a laser power of 3 μW and polarized parallel to the NW axis, with the detection in parallel with the excitation. To ensure that residual stress or any other artefacts do not distort the locally estimated temperature, each temperature point is calculated as the relative shift with respect to a reference spectrum acquired at the same position before the application of the biasing current.

3. Results and discussion

3.1. Device concept and fabrication

Fig. 1 depicts the general layout of the microfabricated device able to integrate and characterize individual nanowires. It features two longitudinal H-shaped 200 μm wide through-all micro-trenches (Fig. 1a). An array of four dodecagonal shaped devices – with 3 mm in diameter each – is patterned inside an 8.5×8.5 mm^2 chip (Fig. 1b). Hence, NW can be grown between opposing pairs of cantilevers across one of the two available micro-trenches, as it is sketched in Fig. 1c. The absence of bulk material underneath the NWs enables the study of structural and thermal properties employing a variety of techniques working in transmission mode including TEM, nano X-ray, or electron diffraction, as well as optical and thermal analysis, *e.g.*, using Raman thermography. Moreover, the selfsame NW studied with these techniques can be fully thermoelectrically characterized. At both sides of the trenches,

a 30 μm-thick suspended platform holds electrical connections and a heater. The former enable four-point electrical contact to the sampled NW from the chip perimeter, where multiple electrical pads are available for external connection. The heaters are designed to create controlled thermal gradients across the trench, with each of them connected by four pads so that – with a calibration of the TCR – it can also serve as a high-precision thermometer. The heater electrical circuit is isolated from the p-doped bulk by a 300 nm Si$_3$N$_4$ layer as it can be observed in the cross-section sketch of the device illustrated in Fig. 1c. A row of 19 cantilever pairs is set along the trench, each of them being mechanically disposable,[29] allowing the elimination of unwanted connections using micro-probes (see Fig. S1c, ESI†).

The MPTD is fabricated using a SOI wafer whose top surface presents the (110) plane as the starting point (Fig. 2a). The fabrication at the component side (top) follows a similar approach as for the thermoelectric microgenerator devices described in our prior works,[22,30] that is, the patterning of a 300 nm silicon nitride layer for electrical insulation of the heater/thermometer elements (Fig. 2c and d) and the subsequent 200 nm metal deposition (W/Ti) of the electrical paths *via* a lift-off process (Fig. 2f). A final SiO$_2$ layer of 1 μm in thickness is deposited on top in order to serve as passivation for the NW growth and as a hard mask for the deep reactive ion etching (DRIE) patterning of the cantilevers (Fig. 2h). After this patterning, a second 500 nm layer of SiO$_2$ is deposited over the component side in order to protect the lateral walls of the cantilevers during the final etching steps on the back side (Fig. 2i). On the back side, a double-layer oxide hard mask – spaced by the 300 nm-thick nitride layer deposited in step c by chemical vapour deposition (CVD) – was required for the fabrication of the staggered pattern using DRIE, as it is illustrated in Fig. 2e. Hence, the suspended 30 μm-thick platforms are fabricated by alternating two levels of photolithography over each oxide layer and their respective DRIE etching. This nitride inter-layer allows the selective removal of the outer oxide mask layer by wet etching (HF) once this mask has served its purpose. Subsequently, the second DRIE mills the bulk, using the buried oxide (BOX) layer as stopping layer (Fig. 2i). Thanks to the passivation of the lateral walls of the cantilevers (step h), over-etching of cantilevers on the component side is avoided should eventual cracks appear in this BOX stressed layer during the final steps of the etching. Finally, cantilevers are released by opening the trench with another wet etching (HF) process (Fig. 2j).

Noteworthy, the chip is fabricated using mainstream silicon technology. Therefore, it can be produced in the large numbers required for comprehensive and high-throughput TE nanomaterial optimizations. In addition, the whole fabrication process is designed without anisotropic etching processes, allowing the chip to be fabricated in any crystallographic direction. This represents a major advantage, as Si NWs' preferential crystallographic growth direction changes with the diameter.[31,32] Therefore, III–V semiconductor[33,34] or silicide[35] NWs with different preferred crystallographic growth directions could also be integrated and tested in this device.
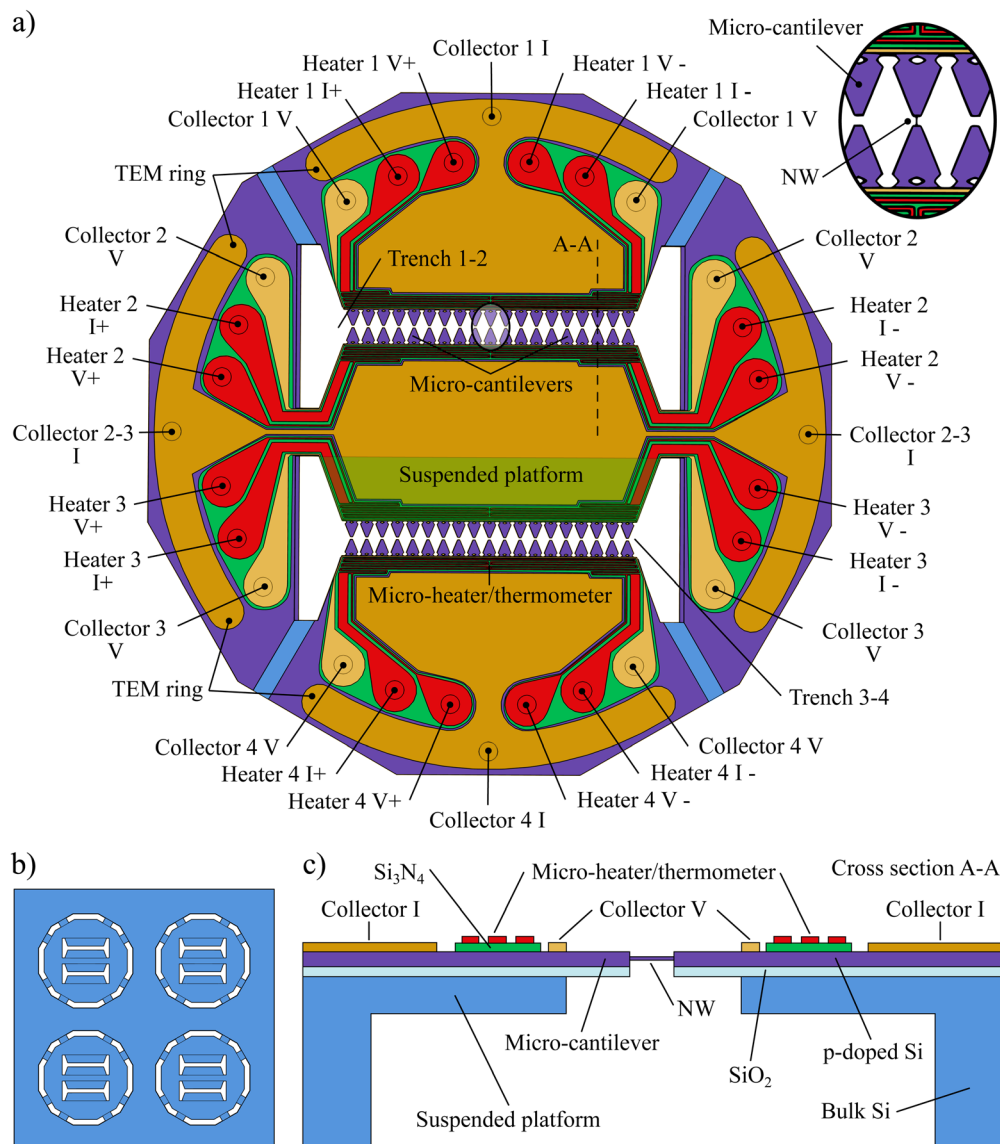
Fig. 1 (a) Overview of the designed device showing the purpose of each pad. The greenish trapezoid represents the surface of one of the four suspended platforms. The red electrical tracks define the four micro-heater/thermometers. The inset at the top right corner zooms the circled area, depicting a possible position of the NW between a pair of disposable arrow-shaped micro-cantilevers (in purple, as the rest of the SOI layer). (b) Bottom side view of the 8.5×8.5 mm^2 chip featuring four dodecagonal devices. (c) Schematic cross-section of the micro-trench. Dimensions are not to scale.

Fig. 3a illustrates the finished device from the components side (top view) while still attached to the chip frame. A remarkably high yield in the fabrication of these devices per processed wafer ($>90\%$) was achieved. The wavy surface visible in the trenches corresponds to the released buried oxide (BOX) layer (used as stopping layer of the bottom dry etching as well). A zoomed view of the micro trench is detailed in Fig. 3b, where the shape of the arrow-like disposable cantilevers patterned on the heavily doped SOI layer of 3 μm in thickness are visible. It is worth noticing how the dodecagonal shape of the device circumscribes a circumference with a diameter of 3 mm. This feature enables the device to fit with standard TEM grid holders as depicted in Fig. 3c, where one of those devices was detached from the chip frame and placed within a TEM sample holder.

Additionally, the location of the current collectors I (see Fig. 1) contacts the chip to the microscope ground, efficiently discharging it.

Prior to the deposition of the Au catalyst nanoparticles used as NW seeds, a second wet HF etch is required to remove the protective SiO$_2$ passivation layer over all metal pads. This etching also removes the remaining buried SiO$_2$ layer, ensuring the thermal insulation of both sides of the trench. The distances between the cantilever pairs ranged from 2 to 20 μm in such a way that NWs with different lengths can be studied. Subsequently, following the procedure described in the experimental Section 2, epitaxial p-doped Si NWs were grown between the cantilever pairs. Fig. 4a and b show SEM images at different magnifications of an epitaxially integrated silicon NW over a pair of cantilevers.
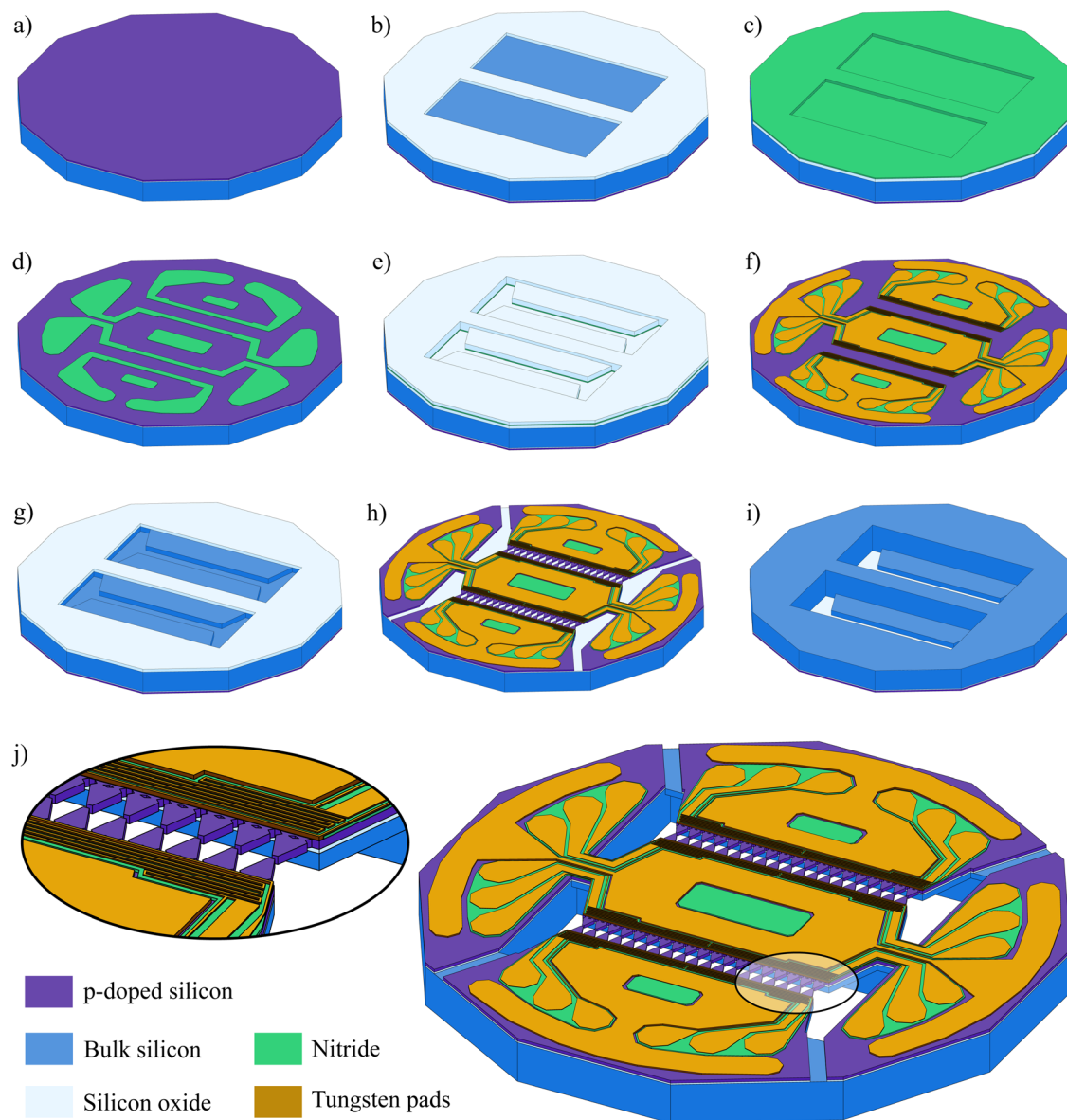
p-doped silicon

Bulk silicon

Silicon oxide

Nitride

Tungsten pads

Fig. 2 Simplified schematic showing the sequence of steps followed during fabrication of the MPTD. (a) Starting SOI substrate. (b) Bottom-side first oxide mask layer deposition and patterning. (c) Silicon nitride CVD deposition on both sides. (d) Patterning of the top-side silicon nitride. (e) Second bottom oxide deposition and patterning. (f) Deposition and patterning of metal layer (Ti + W) *via* lift-off. (g) Photolithography and dry etching of bottom nitride and silicon using the patterned second layer of oxide as a mask. (h) Top-side photolithography patterning of cantilevered trenches and DRIE of doped silicon, followed by the deposition of a double layer of silicon oxide with passivation purposes. (i) Bottom side DRIE using the first bottom oxide layer as mask. (j) Final release of the suspended platforms and cantilevers with HF etching of the buried oxide layer after the CVD-VLS growth and integration of NWs.

This platform hence offers several advantages over the commonly used suspended nitride micro-platforms.[36] Firstly, the integrated growth of the NWs avoids the time-consuming task of transferring NWs from the growth substrate to the microdevice. In addition, the epitaxial growth of the NWs allows to drastically improve the widely known thermal contact issues.[19] Yet, this comes at the price of losing the possibility of removing the electrical contact resistance between NW and bulk as the voltage collectors are in contact with the bulk. Finally, few microdevices featuring suspended nitride membranes have reported the compatibility with transmission experiments.[37]

Still, they require special TEM holders which are not commonly available. In contrast, the presented device can be used in standard TEM holders (Fig. 3c), making it compatible to almost every TEM.

TEM compatibility (Fig. 4c and d) allows to examine the NW structure in detail. High resolution can be achieved thanks to the absence of substrate under the sample. Notably, small Au particles could be resolved with unprecedented detail as illustrated in Fig. 4d. These small gold nano-particles are spilled from the main eutectic droplet during the NW growth and – according to Gadea *et al.*[21] – were responsible for the growth of
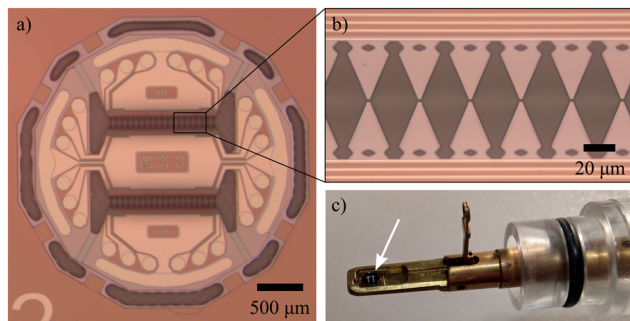
Fig. 3 Optical images showing the fabricated device. (a) Overall view of the device after the last DRIE process performed at the backside, showing the partially opened outer rim. The shape of the 30 μm lateral suspended platforms at each side of the trenches are visible. (b) Detail of one suspended platform, including the microheaters. The compressed layer of buried silicon oxide is visible inside the trench areas. (c) Image of one microdevice on a TEM sample holder. The device is placed face down such that the focal plane is close to that expected for a standard TEM grid.
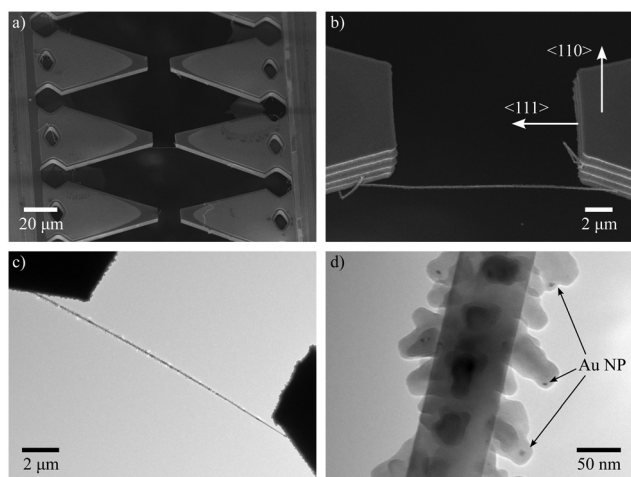

Fig. 4 (a) and (b) SEM images at different magnifications of an integrated Si NW between a pair of cantilevers. The arrows illustrate the crystallographic orientation of the SOI. (c) and (d) TEM images of the same NW. The absence of substrate allows to resolve detail features of the NW morphology, such as the small Au nanoparticles (indicated with arrows) responsible of the secondary lateral growth at the surface of the NW.

the lateral surface protrusions of the NWs fabricated under these conditions. The results of Fig. 4d suggests that this is indeed the mechanism behind the high roughness exhibited by these NWs.

3.2. Thermoelectric characterization

The experimental configuration used to measure the Seebeck coefficient of the integrated wire is sketched in the electrical simulation of the device (Fig. 5a). One of the internal heaters – central top in this case (see Fig. 1a and 3a) – was biased with a current I_{HT}, creating a temperature difference ΔT (under vacuum) across the trench, as depicted in the inset of Fig. 5b. A comprehensive design of the heater area distribution – shifted towards the two sides of the trench – ensured a constant
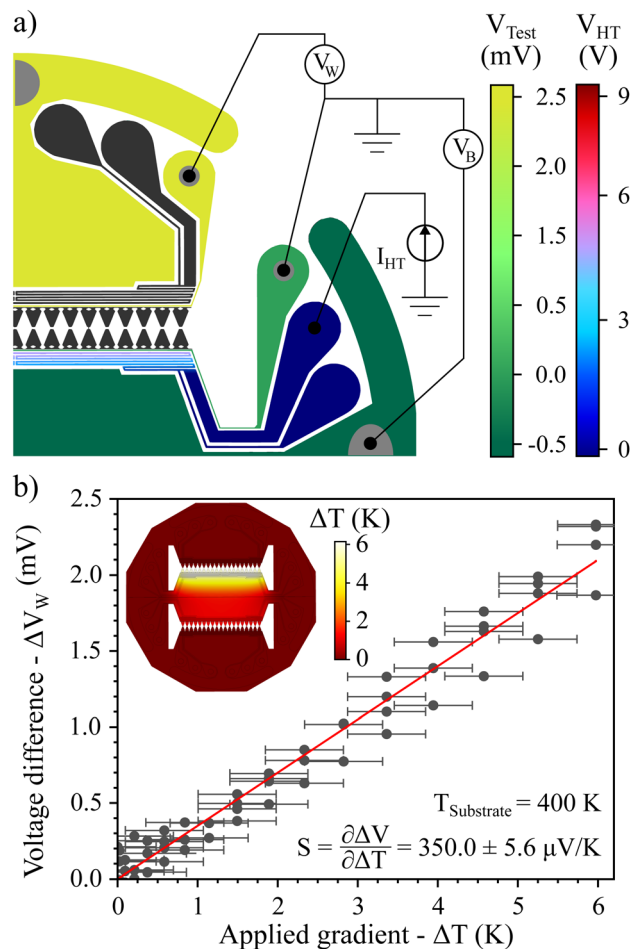

Fig. 5 (a) Schematic of the electrical simulation of the device during a Seebeck measurement. Blue-to-red color-map scales the voltage drop V_{HT} across the central heater, whereas the green-to-yellow scale represents the induced voltages V_{Test} at the collectors metal tracks (plotted in orange in Fig. 1a). A current I_{HT} is supplied to the central heater to create the thermal gradient (see inset in b). This ΔT induces a voltage V_W between the electrical collectors at both sides of the trenches. An oppositely polarized voltage is unavoidably built up across the central heater bulk, represented by V_B. (b) Variation in V_W as a function of the sustained ΔT at 400 K. The slope of the curve is the Seebeck coefficient.

temperature across all cantilevers within a 2.2% precision. During the Seebeck experiment, the ΔT was incrementally increased up to 6 K, reached with 52 mW of dissipated power (4 mA), producing up to 2.1 ± 0.2 mV of thermovoltage (Fig. 5b). The Seebeck coefficient can be then extracted from the slope of the curve, yielding a value of 350.0 ± 5.6 μV K^{-1}.

Notably, the thermovoltage was acquired between the two voltage collectors (V_W in Fig. 5a), which remain insulated over the Si_3N_4 layer except for the area immediately in contact with the cantilevers. This prevents an underestimation of the NW response arising from a negative voltage artefact (denoted as V_B in the sketch) generated by the opposite gradient built up in the doped SOI of the heated platform.

Fig. 6a illustrates how the V collectors allow to perform 4-probe measurements on the NWs avoiding the additional sheet resistance of the device Si layer. Fig. 6b shows the mea-
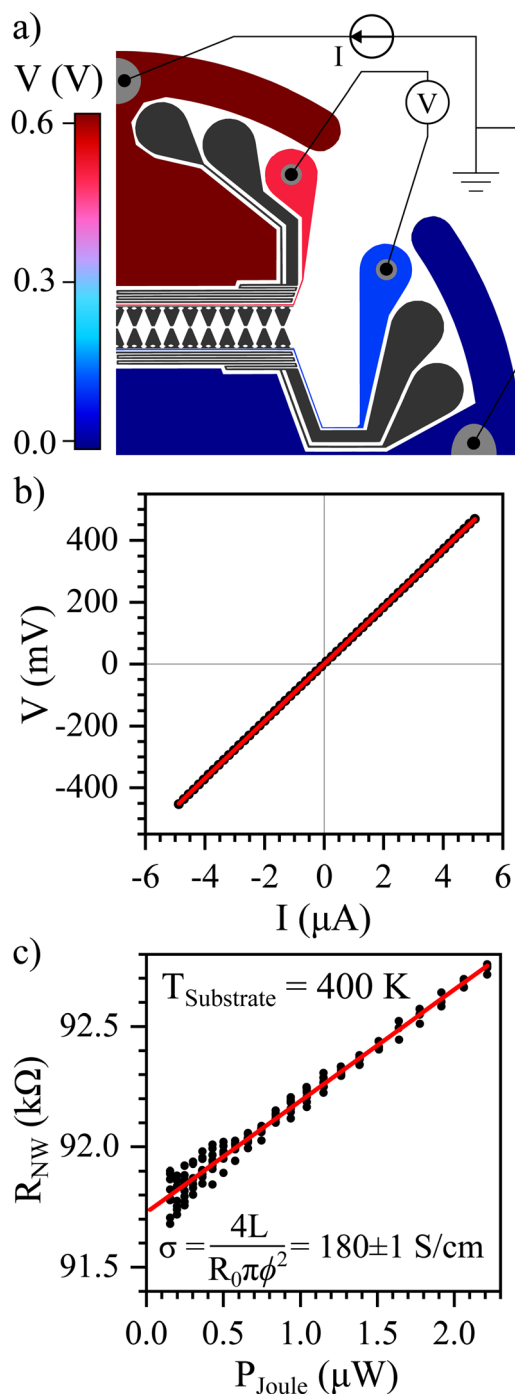
Fig. 6 (a) Schematic of the electric simulation of the device during an I–V test on the NW. A 4-point measurement is carried out using the I and V collectors simultaneously to avoid the effect of the device's p-doped sheet resistance on both sides. (b) Measured I–V curve at 400 K. (c) Corresponding P_{Joule}–R curve, used to compute $R(P = 0)$.

sured I–V curve at 400 K, while the corresponding NW resistance R_{NW} as a function of the Joule dissipated power is depicted in Fig. 6c. A linear dependence with the applied power can be observed, matching the expected behaviour of a self-heating wire with a degenerated (metallic) behaviour, *i.e.* with a roughly constant positive TCR.[26,38] The measured NW featured

a geometric mean diameter of 102.0 ± 0.5 nm and a total length of 13.5 μm. Thus, the NW electrical conductivity σ is estimated at 180.3 ± 1.0 S cm^{-1} and hence the power factor yields 2.21 ± 0.06 mW K^{-2} m^{-1}.

The thermal conductivity κ of the NW is usually the most challenging property to accurately measure, especially when dealing with integrated structures.[21] With micro-Raman thermometry, the shift in the Stokes peak position induced by temperature changes ($\partial\omega_0/\partial T$) can be calibrated (Fig. S2, ESI†) in order to measure the local temperature along the NW.[39] In this work, a calibrated value of $\partial\omega_0/\partial T$ was estimated to be 0.0194 ± 0.0006 cm^{-1} K^{-1} (inset of Fig. S2a, ESI†), being in relatively good agreement with literature data (0.022 ± 0.001 cm^{-1} K^{-1}), where no significant differences were observed compared to bulk silicon.[40,41] This difference might be caused by the NW's thermal expansion being slightly hindered by the fixed side walls, compressing the NW as it tries to expand and therefore avoiding the Raman peak to shift the same way as the freestanding NWs can do.[42]

Fig. 7a shows the obtained Raman shifts with respect to the reference (unheated) spectrum at each position for the case of $T_{Substrate}$ = 300 K for two different applied Joule powers, *i.e.* with the current bias self-heating the NW. Fig. 7b illustrates the optical images of the relative laser position y with respect to the NW longitudinal axis. During the experiment the laser power was kept to 3 μW, low enough to avoid noticeable laser heating but still sufficient to resolve the signal (see inset of Fig. S2b, ESI†). The right axis depicts the correspondence with the temperature rise using the calibrated $\partial\omega_0/\partial T$. A well-defined parabolic profile is observed for both applied Joule powers, being the maximum temperature directly proportional to the dissipated power. This is indeed the expected temperature profile of a homogeneously self-heated wire (under vacuum conditions) as it was described by Völklein *et al.*:[43]

$$\Delta T_{Joule}(y) = \frac{P_{Joule}}{2\kappa AL}\left[\left(\frac{L}{2}\right)^2 - y^2\right] \tag{1}$$

where $P_{Joule} = V\cdot I$ is the dissipated power, A is the cross sectional area of the wire, L is its length, and y is the position along the NW being $y = 0$ the central point. Fitting the temperature profiles with eqn (1) allows determining κ. A value of 24.3 ± 1.7 W Km^{-1} was fitted for the high power case (15.0 μW) with the substrate at room temperature (300 K). However, these estimated values correspond to the average temperature rise of the wire $\overline{\Delta T} = 3/2\Delta T_{max}$.[43] In the particular case depicted in Fig. 7a, this corresponds to average NW temperatures of 353 and 398 K for the low and high power cases, respectively. Fig. 7c illustrates the temperature dependence of κ. As it can be noticed, a linear trend is found when κ is plotted as a function of the average $\overline{\Delta T}$. Results match a purely electrical self-heating experiment depicted as black circles in Fig. 7c. Details of this standard experimental approach can be found elsewhere.[26] In addition, the magnitude of κ can be reasonably modelled (solid line in Fig. 7c) by considering the phonon-boundary scattering proposed by Yang *et al.*[44] This approach assumes a surface
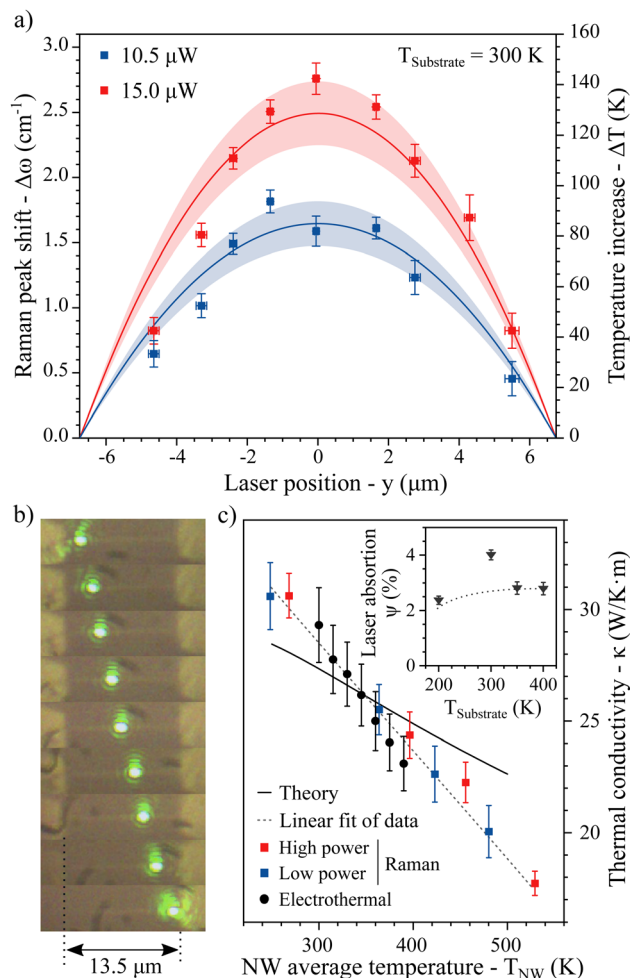
Fig. 7 (a) Raman peak shifts and corresponding temperature rise produced by two Joule heating powers of 10.5 μW and 15 μW (blue and red, respectively) measured along the NW axis. The solid line represents the fit of the data using eqn (1) and the shaded area the confidence interval (95%). (b) Sequence of optical microscope images showing the laser position along the NW. The central point (5th image) was used during the power tests (Fig. S2, ESI†) as it is the most sensitive position to heating. (c) Resulting thermal conductivity values as a function of the NW average temperature. Black circles show the obtained results using the self-heating method.[26] The inset shows the calculated laser absorption coefficient using eqn (3).

scattering rate beyond the fully diffusive Casimir limit, where phonons are trapped in multiple reflections at the protuberances of the NW surface (see Fig. 4d). However, experimental data show a higher temperature dependence with respect to the model, pointing to a possible underestimation of the Umklapp scattering processes together with an overestimation of the boundary scattering in the latter.

Moreover, it is remarkable to observe the absence of a sharp temperature step between the nanowire thermal profile and the bulk temperature. This constitutes direct proof of the negligible thermal contact resistance between NW and bulk as a consequence of the epitaxial growth of the NWs. This result agrees with the estimations of Gadea et al.[21] using the transmission line method and our independent verification using Scanning Thermal Microscope experiments (SthM).[45]

It is also worth noticing that no error in the measurement of κ is derived from the estimation of the laser power absorption coefficient ψ – a very challenging parameter to measure experimentally –,[17] as the heating is done purely electrically. Indeed, ψ can be here estimated by comparing the ΔT profile expected when using electrical heating (eqn (1)) with the behaviour when using laser heating as a (quasi) punctual heat source as proposed by Soini et al.:[27]

$$\Delta T_{\mathrm{Laser}}(y) = \frac{P_{\mathrm{Laser}} \eta \psi}{\kappa A L} \left[\left(\frac{L}{2}\right)^2 - y^2 \right] \qquad (2)$$

with η being the combined transmission efficiency of the objective and cryostat window, calibrated as 65.6% for the used laser wavelength (532 nm). Then, the ratio of both ΔT profiles can be re-arranged as:

$$\psi = \frac{1}{2\eta} \cdot \frac{\Delta T_{\mathrm{Laser}}}{\Delta T_{\mathrm{Joule}}} \cdot \frac{P_{\mathrm{Joule}}}{P_{\mathrm{Laser}}} = \frac{1}{2\eta} \cdot \frac{\partial T/\partial P|_{\mathrm{Laser}}}{\partial T/\partial P|_{\mathrm{Joule}}} \qquad (3)$$

where ψ can then be deduced from the ratio of temperature increase by laser heating $\partial T/\partial P|_{\mathrm{Laser}}$ compared to the Joule heating counterpart $\partial T/\partial P|_{\mathrm{Joule}}$. Both values can be experimentally fitted from the calibration power curves shown in Fig. S2a and b (ESI†), respectively. The inset of Fig. 7c shows the estimated ψ ranges from 2.2 to 4.1%. This rather low absorption efficiency further validates the approach of neglecting the power dissipated by the laser while mapping the temperature profiles illustrated in Fig. 7a in comparison with the dissipated Joule heat. Noteworthy, these obtained values include the geometrical effects caused by the beam spot being larger than the NW diameter. Therefore, ψ is calculated from the total laser power input in the cryostat, not just the power fraction directly heating the NW. As discussed by Swinkels et al.,[17] this ensures that ψ captures all diffractive interactions between the incoming photons and a sub-wavelength body, i.e. the NW. In this regime, photons could be absorbed beyond the NW cross-section area, and other photons directly hitting the NW might not irradiate it. However, these values are not directly comparable with those obtained from Mie-type solutions to Maxwell's equations as proposed by Doerk et al.[39] or Anaya et al.,[46] which account for the ratio of the absorption cross-section over the projected area of the NW, thus not taking into account for the Gaussian and finite shape of the photon source.

Table 1 summarizes the obtained results for the studied nanowire. σ and S values measured are both consistent with a NW with doping concentration in the range of 1.5×10^{19} – 3.5×10^{19} cm^{-3},[26] which was the level targeted with the diborane partial pressure used during the growth of the NWs (see Section 2). κ obtained is consistent between the two techniques used in this work, and the trend with temperature

Table 1 Summary of thermoelectric properties obtained for the studied NW at 400 K

L (μm)	ϕ (nm)	σ (S cm^{-1})	S (μV K^{-1})	k (W mK^{-1})	zT (—)
13	102.0 ± 0.5	180.0 ± 1.0	350.0 ± 5.6	24.3 ± 1.7	0.036 ± 0.002

is negative, as expected from the increasing prevalence of Umklapp scattering in NWs of this diameter.[13] The obtained absolute values are comparable to what is expected for a very rough silicon nanowire of this diameter ($\sim$27 W Km^{-1}).[47,48] Overall, the resulting figure of merit for the NW at a typical thermoelectric operation temperature of 400 K is 0.036 $\pm$ 0.002, which is also consistent with previously reported values.[21]

Overall, this device will ease the optimization of nanowires for thermoelectric and optoelectronic applications, enabling their complete characterization within a single device. In particular, it will be especially interesting for the study of porous silicon nanowires,[49–51] where proper characterization of the porosity typically requires high-resolution TEM. Additionally, structural characterization in synchrotron X-ray sources typically works in transmission mode.[52] Hence, the absence of supporting substrate is particularly useful in this case as well. This device is also appealing for its use in the study of nanowires with ion-induced defects for the enhancement of phonon scattering.[53,54] In all these possible measurements, *in situ* tests would be straightforwardly implemented similarly to the combined electro-opitcal measurements described in Fig. 7b. This can be particularly interesting for SthM experiments with simultaneous electrical and/or thermal excitation.[45] This constitutes a further degree of freedom when planning these experiments.

4. Conclusions

This work presents the complete morphological, structural, and thermoelectric characterization of the selfsame individual epitaxially integrated nanowire. This study is enabled by the use of a unique and versatile multi-purpose test microdevice. Such device features an architecture without substrate underneath the sample, enabling transmission experiments for detailed morphological characterization, including TEM. The selfsame nanowire can then be electrically and thermally characterized, obtaining the whole set of properties from the same sample. Additionally, the chip can be fabricated in any crystallographic direction, thus enabling its potential use for other nanowire materials. Subsequently, the complete characterization of a fully epitaxially integrated rough Si nanowire using SEM, TEM, electrical and Raman techniques was carried out. Remarkably, no thermal contact resistance was observed after resolving the temperature profile along the nanowire, confirming our previous independent experiments. In addition, the optical absorption coefficient of the nanowires was estimated by combining Joule and laser heating experiments. Overall, this device will ease the optimization of nanowires for thermoelectric and optoelectronic applications, enabling their complete characterization within a single device. This constitutes a further degree of freedom when planning these experiments.

Author contributions

J. M. S. G.: conceptualization, investigation, validation, data curation, formal analysis, visualization, software, writing – original draft; Y. K.: investigation, methods, writing – review and editing; S. T.: investigation, data curation, writing – original draft; N. A.: conceptualization, methods; N. F.: investigation; M. S.: investigation, methods, resources, writing – review and editing; L. F.: resources, funding acquisition, writing – review and editing; A. M.: resources, funding acquisition, writing – review and editing; A. T.: resources, funding acquisition, writing – review and editing; I. Z.: conceptualization, funding acquisition, writing – review and editing.

Conflicts of interest

There are no conflicts to declare.

Acknowledgements

References

1 C. Jia, Z. Lin, Y. Huang and X. Duan, Nanowire Electronics: From Nanoscale to Macroscale, *Chem. Rev.*, 2019, **119**, 9074–9135.

2 Y. Zhang, J. Wu, M. Aagesen and H. Liu, III–V nanowires and nanowire optoelectronic devices, *J. Phys. D: Appl. Phys.*, 2015, **48**, 463001.

3 L. N. Quan, J. Kang, C.-Z. Ning and P. Yang, Nanowires for Photonics, *Chem. Rev.*, 2019, **119**, 9153–9169.

4 M. Y. Swinkels and I. Zardo, Nanowires for heat conversion, *J. Phys. D: Appl. Phys.*, 2018, **51**, 353001.

5 N. I. Goktas, P. Wilson, A. Ghukasyan, D. Wagner, S. McNamee and R. R. LaPierre, Nanowires for energy: A review, *Appl. Phys. Rev.*, 2018, **5**, 041305.

6 J. M. Sojo Gordillo, A. Morata, C. D. Sierra, M. Salleras, L. Fonseca and A. Tarancon, Recent advances in silicon-based nanostructures for thermoelectric applications, *APL Mater.*, 2023, **11**, 040702.

7 E. Hittinger and P. Jaramillo, Internet of things: Energy boon or bane?, *Science*, 2019, **364**, 326–328.

8 A. Tarancon, Powering the IoT revolution with heat, *Nat. Electron.*, 2019, **2**, 270–271.

9 O. H. Ando Junior, A. L. Maran and N. C. Henao, A review of the development and applications of thermoelectric micro-generators for energy harvesting, *Renewable Sustainable Energy Rev.*, 2018, **91**, 376–393.

10 Q. Zhang, K. Deng, L. Wilkens, H. Reith and K. Nielsch, Micro-thermoelectric devices, *Nat. Electron.*, 2022, **5**, 333–347.

11 M. Haras and T. Skotnicki, Thermoelectricity for IoT – a review, *Nano Energy*, 2018, **54**, 461–476.

12 P. Kim, L. Shi, A. Majumdar and P. L. McEuen, Thermal Transport Measurements of Individual Multiwalled Nano-tubes, *Phys. Rev. Lett.*, 2001, **87**, 215502.

13 D. Li, Y. Wu, P. Kim, L. Shi, P. Yang and A. Majumdar, Thermal conductivity of individual silicon nanowires, *Appl. Phys. Lett.*, 2003, **83**, 2934–2936.

14 A. I. Hochbaum, R. Chen, R. D. Delgado, W. Liang, E. C. Garnett, M. Najarian, A. Majumdar and P. Yang, Enhanced thermoelectric performance of rough silicon nanowires, *Nature*, 2008, **451**, 163–167.

15 P. Ferrando-Villalba, A. F. Lopeandia, L. Abad, J. Llobet, M. Molina-Ruiz, G. Garcia, M. Gerboles, F. X. Alvarez, A. R. Goñi, F. J. Munoz-Pascual and J. Rodriguez-Viejo, In-plane thermal conductivity of sub-20 nm thick suspended mono-crystalline Si layers, *Nanotechnology*, 2014, **25**, 185402.

16 S. Shin, M. Elzouka, R. Prasher and R. Chen, Far-field coherent thermal emission from polaritonic resonance in individual anisotropic nanoribbons, *Nat. Commun.*, 2019, **10**, 1–11.

17 M. Y. Swinkels, A. Campo, D. Vakulov, W. Kim, L. Gagliano, S. E. Steinvall, H. Detz, M. De Luca, A. Lugstein, E. Bakkers, I. Fontcuberta, A. Morral and I. Zardo, Measuring the Optical Absorption of Single Nanowires, *Phys. Rev. Appl.*, 2020, **14**(2), 024045.

18 D. Vakulov, *et al.*, Ballistic Phonons in Ultrathin Nanowires, *Nano Lett.*, 2020, **20**, 2703–2709.

19 M. Y. Swinkels, M. R. Van Delft, D. S. Oliveira, A. Cavalli, I. Zardo, R. W. Van Der Heijden and E. Bakkers, Diameter dependence of the thermal conductivity of InAs nanowires, *Nanotechnology*, 2015, **26**, 385401.

20 S. Yazji, M. Y. Swinkels, M. De Luca, E. A. Hoffmann, D. Ercolani, S. Roddaro, G. Abstreiter, L. Sorba, E. P. A. M. Bakkers and I. Zardo, Assessing the thermoelectric proper-ties of single InSb nanowires: the role of thermal contact resistance, *Semicond. Sci. Technol.*, 2016, **31**, 064001.

21 G. Gadea, J. M. Sojo Gordillo, M. Pacios Pujado, M. Salleras, L. Fonseca, A. Morata and A. Tarancon Rubio, Enhanced thermoelectric figure of merit of individual Si nanowires with ultralow contact resistances, *Nano Energy*, 2020, **67**, 104191.

22 J. M. Sojo-Gordillo, C. D. Sierra, G. Gadea Diez, J. Segura-Ruiz, V. Bonino, M. Nunez Eroles, J. C. Gonzalez-Rosillo, D. Estrada-Wiese, M. Salleras, L. Fonseca, A. Morata and A. Tarancon, Superior Thermoelectric Performance of SiGe Nanowires Epitaxially Integrated into Thermal Micro-Harvesters, *Small*, 2023, **19**, 2206399.

23 G. Gadea, A. Morata, J. D. Santos, D. Davila, C. Calaza, M. Salleras, L. Fonseca and A. Tarancon, Towards a full integration of vertically aligned silicon nanowires in MEMS using silane as a precursor, *Nanotechnology*, 2015, **26**, 195302.

24 A. I. Hochbaum, R. Fan, R. He and P. Yang, Controlled growth of Si nanowire arrays for device integration, *Nano Lett.*, 2005, **5**, 457–460.

25 G. Gadea, *Integration of Si/Si-Ge nanostructures in micro-thermoelectric generators*, PhD thesis, Universidad de Barce-lona, 2017.

26 J. M. Sojo-Gordillo, D. Estrada-Wiese, C. Duque-Sierra, G. Gadea Diez, M. Salleras, L. Fonseca, A. Morata and A. Tarancon, Tuning the thermoelectric properties of boron-doped silicon nanowires integrated into a micro-harvester, *Adv. Mater. Technol.*, 2022, **7**(10), 2101715.

27 M. Soini, I. Zardo, E. Uccelli, S. Funk, G. Koblmuller, I. Fontcuberta, A. Morral and G. Abstreiter, Thermal con-ductivity of GaAs nanowires studied by micro-Raman spectroscopy combined with laser heating, *Appl. Phys. Lett.*, 2010, **97**, 16–18.

28 S. Yazji, E. A. Hoffman, D. Ercolani, F. Rossella, A. Pitanti, A. Cavalli, S. Roddaro, G. Abstreiter, L. Sorba and I. Zardo, Complete thermoelectric benchmarking of individual InSb nanowires using combined micro-Raman and electric trans-port analysis, *Nano Res.*, 2015, **8**, 4048–4060.

29 F. W. DelRio, R. F. Cook and B. L. Boyce, Fracture strength of micro- and nano-scale silicon components, *Appl. Phys. Rev.*, 2015, **2**, 021303.

30 D. Estrada-Wiese, J.-M. Sojo, M. Salleras, J. Santander, M. Fernandez-Regulez, I. Martin-Fernandez, A. Morata, L. Fonseca and A. Tarancon, Harvesting performance of a planar thermoelectric microgenerator with a compact design, 2021, IEEE 20th International Conference on Micro and Nanotechnology for Power Generation and Energy Conversion Applications (PowerMEMS), 2021, pp. 108–111.

31 V. Schmidt, S. Senz and U. Gosele, Diameter-dependent growth direction of epitaxial silicon nanowires, *Nano Lett.*, 2005, **5**, 931–935.

32 C. X. Wang, M. Hirano and H. Hosono, Origin of Diameter-Dependent Growth Direction of Silicon Nanowires, *Nano Lett.*, 2006, **6**, 1552–1555.

33 A. L. Roest, M. A. Verheijen, O. Wunnicke, S. Serafin, H. Wondergem and E. P. A. M. Bakkers, Position-controlled epitaxial III - V nanowires on silicon, *Nanotechnology*, 2006, 271–275.

34 H. Zeng, X. Yu, H. A. Fonseka, G. Boras, P. Jurczak, T. Wang, A. M. Sanchez and H. Liu, Preferred growth direction of III–V nanowires on differently oriented Si substrates, *Nanotech-nology*, 2020, **31**, 475708.

35 C. Y. Yang, S. M. Yang, Y. Y. Chen and K. C. Lu, Fabrication and Physical Properties of Single-Crystalline Beta-FeSi2 Nanowires, *Nanoscale Res. Lett.*, 2020, **15**(1), 197.

36 L. Shi, D. Li, C. Yu, W. Jang, D. Kim, Z. Yao, P. Kim and A. Majumdar, Measuring Thermal and Thermoelectric Prop-erties of One-Dimensional Nanostructures Using a Micro-fabricated Device, *J. Heat Transfer*, 2003, **125**, 881.

37 G. de Vito, D. M. Koch, G. Raciti, J. M. Sojo-Gordillo, A. Nigro, R. Swami, Y. Kaur, M. Y. Swinkels, W. Huang, T. Paul, M. Calame and I. Zardo, Suspended micro thermometer for anisotropic thermal transport measurements, *Int. J. Heat Mass Transfer*, 2024, **224**, 125302.

38 G. Pennelli, E. DImaggio and M. MacUcci, Note: Improvement of the 3ω thermal conductivity measurement technique for its application at the nanoscale, *Rev. Sci. Instrum.*, 2018, **89**, 16102–16105.

39 G. S. Doerk, C. Carraro and R. Maboudian, Single Nanowire Thermal Conductivity Measurements by Raman Thermography, *ACS Nano*, 2010, **4**, 4908–4914.

40 T. R. Hart, R. L. Aggarwal and B. Lax, Temperature dependence of Raman scattering in silicon, *Phys. Rev. B: Solid State*, 1970, **1**, 638–642.

41 G. S. Doerk, C. Carraro and R. Maboudian, Temperature dependence of Raman spectra for individual silicon nanowires, *Phys. Rev. B: Condens. Matter Mater. Phys.*, 2009, **80**, 1–4.

42 K. F. Murphy, B. Piccione, M. B. Zanjani, J. R. Lukes and D. S. Gianola, Strain- and defectmediated thermal conductivity in silicon nanowires, *Nano Lett.*, 2014, **14**, 3785–3792.

43 F. Volklein, H. Reith, T. W. Cornelius, M. Rauber and R. Neumann, The experimental investigation of thermal conductivity and the Wiedemann-Franz law for single metallic nanowires, *Nanotechnology*, 2009, **20**, 325706.

44 H.-Y. Yang, Y.-L. Chen, W.-X. Zhou, G.-F. Xie and N. Xu, Ultra-low thermal conductivity of roughened silicon nanowires: Role of phonon-surface bond order imperfection scattering, *Chin. Phys. B*, 2020, 0–14.

45 J. M. Sojo-Gordillo, G. Gadea Diez, D. Renahy, M. Salleras, C. Duque-Sierra, P. Vincent, L. Fonseca, P.-O. Chapuis, A. Morata, S. Gomès and A. Tarancón, Local heat dissipation and elasticity of suspended silicon nanowires revealed by dual scanning electron and thermal microscopies, *Small*, 2023, 2305831.

46 J. Anaya, A. Torres, A. Martin-Martin, J. Souto, J. Jimenez, A. Rodriguez and T. Rodriguez, Study of the temperature

47 L. N. Maurer, Z. Aksamija, E. B. Ramayya, A. H. Davoody and I. Knezevic, Universal features of phonon transport in nanowires with correlated surface roughness, *Appl. Phys. Lett.*, 2015, **106**, 133108.

48 J. Lim, K. Hippalgaonkar, S. C. Andrews, A. Majumdar and P. Yang, Quantifying surface roughness effects on phonon transport in silicon nanowires, *Nano Lett.*, 2012, **12**, 2475–2482.

49 K. Valalaki, P. Benech and A. Galiouna Nassiopoulou, High Seebeck Coefficient of Porous Silicon: Study of the Porosity Dependence, *Nanoscale Res. Lett.*, 2016, **11**(1), 201.

50 P. Ferrando-Villalba, L. D'Ortenzi, G. G. Dalkiranis, E. Cara, A. F. Lopeandia, L. Abad, R. Rurali, X. Cartoixa, N. De Leo, Z. Saghi, M. Jacob, N. Gambacorti, L. Boarino and J. Rodriguez-Viejo, Impact of pore anisotropy on the thermal conductivity of porous Si nanowires, *Sci. Rep.*, 2018, **8**, 12796.

51 L. Yang, D. Huh, R. Ning, V. Rapp, Y. Zeng, Y. Liu, S. Ju, Y. Tao, Y. Jiang, J. Beak, J. Leem, S. Kaur, H. Lee, X. Zheng and R. S. Prasher, High thermoelectric figure of merit of porous Si nanowires from 300 to 700 K, *Nat. Commun.*, 2021, **12**, 3926.

52 J. Segura-Ruiz, G. Martinez-Criado, C. Denker, J. Malindretos and A. Rizzi, Phase Separation in Single In x Ga 1- x N Nanowires Revealed through a Hard X-ray Synchrotron Nanoprobe, *Nano Lett.*, 2014, **14**, 1300–1305.

53 N. S. Bennett, N. M. Wight, S. R. Popuri and J. W. G. Bos, Efficient thermoelectric performance in silicon nanofilms by vacancy-engineering, *Nano Energy*, 2015, **16**, 350–356.

54 N. S. Bennett, D. Byrne, A. Cowley and N. Neophytou, Dislocation loops as a mechanism for thermoelectric power factor enhancement in silicon nano-layers, *Appl. Phys. Lett.*, 2016, **109**(17), 173905.

distribution in Si nanowires under microscopic laser beam excitation, *Appl. Phys. A: Mater. Sci. Process.*, 2013, **113**, 167–176.